Supporting Information

Deo et al. 10.1073/pnas.1218154110

SI Results

We have conducted experiments to determine the kinetics of activation and the rectification indices of the WT and E299V mutant channels, as presented in Fig S2. Currents were recorded in the presence of 5.4 mM extracellular K^+ in response to voltage steps from −30 mV holding potential to −120 mV in 10-mV increments. Fig. S2*A* shows representative superimposed traces for WT, E299V, and WT/E299V. As expected, for all three constructs, channel activation observed at hyperpolarized potentials displayed a characteristic pseudoinstantaneous phase (1), followed by a much slower monoexponential current increase (Fig. S2*A*). During the initial pseudoinstantaneous phase, E299V had faster activation than WT. However, the activation was slower when WT and E299V were coexpressed. During the slower phase, the WT current already decayed at a time when E299V was still activating slowly; from this long-term point, the WT/E299V (no decay, no slow activation) is between the WT and E299V. Currents were fitted with monoexponential functions using the first 20 ms in each current recording to determine the activation time constants and their voltage dependence (Fig. S2*B*) according to the protocol described by Panama et al. (2), which included only the initial component of activation. The data in Fig. S2 *A* and *B* suggest that the E299V and WT isoforms form heteromultimeric complexes (as demonstrated by the coimmunoprecipitation data shown in Fig. 2*C*) and that their interaction somehow impairs function, whereas the homomeric assembly of E299V mutant proteins actually results in a gain of function. In Fig. S2*C*, the rectification index was calculated as the ratio of current amplitudes measured 380–400 ms after the onset of step pulses to 0 mV and −100 mV. The graph shows that the E299V mutation impairs rectification substantially and that the heteromultimeric WT/E299V complex partially rescues rectification. These results confirm the previously demonstrated importance of the negative charge of E299 in the Kir2.1 sequence in controlling inward rectification (3).

SI Materials and Methods

Site-Directed Mutagenesis. The E299V mutation in *KCNJ2*, the gene that encodes the strong inward rectifier K^+ channel protein (Kir2.1), was engineered into WT cDNA cloned in pcDNA3.1 (Invitrogen). Site-directed mutagenesis was carried out using a PCR-based strategy with PfuTurbo DNA polymerase (QuikChange; Stratagene). The HA epitope (YPYDVPDYA) (4) and the decapeptide sequence from c-myc protein (EQKLISEEDL) (5) were introduced into the *KCNJ2* cDNA (WT and mutants) between residues Asp-114 and Ala-115 (extracellular loop between TM1 and TM2) with the following primers: F_HA_5′TACCCATACGACGTCCCAGACTACGCTGCATCCAAAGAGGGCAAAGCT-3′ and R_HA_5′_AGCGTAGTCTGGGACGTCGTATGGGTAATCCAGGTCCCCATGGAGCAG-3′; F_Myc_5′-GAACAAAAACTTATTTCTGAAGAAGATCTGGCATCCAAAGAGGGCAAAGCT-3′ and R_Myc_5′-CAGATCTTCTTCAGAAATAAGTTTTTGTTCATCCAGGTCCCCATGGAGCAG-3′. All of the constructs were confirmed by sequencing analysis of the entire cDNA.

Transfection in HEK293 Cells. HEK 293 cells were transfected with 1.6 μg of plasmid DNA of Kir2.1-WT or Kir2.1-E299V mutant using Effectene (Qiagen), as directed by the manufacturer. To mimic the heterozygous substrate, 0.8 μg of each plasmid was transfected. In addition, 0.8 μg of GFP cDNA was cotransfected to serve as a reporter gene.

SDS/PAGE and Western Blotting. The expression analysis of WT-*KCNJ2* and E299V-*KCNJ2* was performed by Western blot. HEK293 cells were transiently transfected by Effectene (Qiagen) with 1 μg/dish of pCDNA3.1-WT-KCNJ2 or pCDNA3.1-E299V-KCNJ2. Forty-eight hours after transfection eight 100-mm dishes of transfected cells were placed on ice, washed with PBS, and lysed with 1 mL of lysis buffer with protease inhibitor mixture (Biovision Research Products). The extractions were performed in accordance with the manufacturer's instruction. The different fractions (total, cytoplasmic, and plasma membrane fractions) were collected and quantified (BCA protein assay kit; Thermo Scientific Pierce). Samples containing 15 μg of total protein were loaded on a 4–12% linear gradient polyacrylamide gel (Invitrogen) and run at 200 mV for 1 h at room temperature. The proteins were transferred to a nitrocellulose membrane (Invitrogen) at 30 mV for 2 h at 4 °C. Nonspecific binding was blocked with 3% (wt/vol) nonfat dry milk in Tris-buffered saline with Tween (TBS-T). The membrane was then incubated for 1 h at room temperature with a rabbit anti-KCNJ2 antibody (1:1,000; Chemicon) and anti–Pan-Cadherin (1:2,000, Sigma-Aldrich) followed by TBS-T washes. The blot was incubated with a HRP-conjugated anti-rabbit antibody (1:3,500; Promega). The detection was performed with the Supersignal West Pico Chemiluminescent substrate (Pierce) and exposed using X-ray film (Kodak).

Immunofluorescence. Immunofluorescence microscopy was used to detect the presence of KCNJ2 protein at the plasma membrane of HEK293 cells. Transfections were performed with 0.3 μg/well of HA-WT-KCNJ2 or Myc-E299V-KCNJ2 plasmid DNA in a 24-well tissue culture plate. After 48 h, the cells were washed with PBS and fixed with 3.7% formaldehyde for 10 min, followed by PBS washes. The samples were blocked with 10% donkey serum (Sigma-Aldrich) for 1 h, followed by an incubation with mouse anti-HA and anti–c-myc antibodies, respectively (1:100; Sigma-Aldrich) for 1 h at room temperature. Cells were washed with PBS and incubated with Dy-Light- 594-conjugated donkey anti-mouse IgG (Jackson Laboratories). The coverslips were mounted using fluorescent mounting medium (Dako). Confocal microscopy was performed with a Leica TCS-SP2 digital scanning confocal microscope equipped with a HCX PL APO 40×, n.a.1.25 oil-immersion objective. We used the He/Ne laser line at 580–630 nm. The pinhole diameter was kept at Airy 1. Images were exported to Adobe Photoshop (Adobe Systems).

Immunoprecipitation. The protein–protein interaction was studied with coimmunoprecipitation with Kir2.1 subunits tagged with different epitopes. HEK293 cells were transiently transfected by Effectene (Qiagen) with 1 μg of DNA for each plasmid in the following combinations: HA-WT-KCNJ2 + Myc-E299V-KCNJ2, HA-E299V-KCNJ2 + Myc-E299V-KCNJ2, and HA-WT-KCNJ2 + Myc-WT-KCNJ2. Forty-eight hours after transfection the cells were placed on ice, washed with PBS, and lysed in the presence of protease inhibitors in accordance with the manufacturer's instructions (Dynabeads coimmunoprecipitation kit; Invitrogen). The immunoprecipitation and the immunoblot were performed with the anti-Myc and anti-HA antibody (Sigma-Aldrich).

Cellular Electrophysiology. Functional characterization of WT and mutant channels was performed by patch clamp using an Axopatch 700B Amplifier (Axon Instruments). Current recordings were performed at room temperature. The recording solution contained (in mmol/L) NaCl 135, KCl 4.8, $CaCl_2$ 1.8, $MgCl_2$ 1,

Glucose 10, and Hepes 5; the pH was adjusted to 7.4 with NaOH. The micropipette solution contained (in mmol/L) KAsp 130, KCl 15, $MgCl_2$ 1, K_2-ATP 2, and Hepes 5; the pH was adjusted to 7.4 with KOH. To show Kir2.1 specificity, 1 mmol/L $BaCl_2$ was added to the bath solution to block the inward rectifying current. I_{K1} data were plotted as barium-sensitive currents. Data were adjusted for the liquid junction potential (15 mV) and presented as means ± SEM. Two-tailed Student *t* test was used to compare means; $P < 0.05$ was considered statistically significant.

Numerical Methods. ***Human ventricular myocyte.*** A mathematical model of the normal human ventricular myocyte (VM) by O'Hara et al. (6) was implemented to simulate the cardiac action potential. The formulation for the fast sodium current in the original model was replaced with that of a mammalian ventricular myocyte model (LRd 1999, ref. 7) to achieve propagation in 2D cardiac tissue. The mathematical formulation for I_{K1} in the control action potential was modified to fit current densities obtained from WT Kir2.1 channels, expressed in HEK cells by scaling them to match the maximum outward current amplitude of the original O'Hara model. Here the modified model is referred to as ORd. Then, the same scaling factor was used to fit the current density data in homozygous (E299V) and heterozygous (WT/E299V) mutant Kir2.1 channels, recorded in HEK cells (Fig. S2*A*). Previously reported SQT3 WT/D172N and D172N mutations (8) were implemented similarly (Fig. S2*B*) to compare the ECG morphologies and arrhythmogenic properties of the mutated ventricles. The following equations were fitted to reproduce the I_{K1} characteristics in the mutations studied:

Control

$$I_{K1} = \frac{0.24731(V - E_K)}{0.86426 + e^{0.09014(V - E_K)}} - 0.06519$$

WT/E299V

$$I_{K1} = \frac{0.11905(V - E_K + 2.4)}{0.04092 + e^{0.01732(V - E_K)}} - 0.36212$$

E299V

$$I_{K1} = 0.06634(V - E_K + 6.5) - 2.44009 \times 10^{-4}(V - E_K)^2 - 0.51383$$

WT/D172N

$$I_{K1} = \frac{1.2645(V - E_K)}{4.0041 + e^{0.0841(V - E_K)}} - 0.2172$$

D172N

$$I_{K1} = \frac{7.7402(V - E_K)}{21.5492 + e^{0.1052(V - E_K)}} - 0.2737.$$

Here E_K is the reversal potential for K^+ ions and V is the transmembrane voltage.

Human atrial cell. The arrhythmogenic effects of WT/E299V and E299V mutations were also studied in human atria by conducting simulations using the Grandi-Pandit model (9) (referred to as the GP model) of human atrial cells. The formulation for the fast sodium current in the original model was also replaced with that of a mammalian ventricular myocyte model (LRd 1999, ref. 7) to achieve propagation in 2D cardiac tissue. The maximum upstroke velocity (dV/dt_{max}) was adjusted to 205 mV/ms, which resulted in a conduction velocity of 0.52 m/s (10, 11). Then the I_{K1} model equations were fitted to the current densities obtained from WT Kir2.1 channels, expressed in HEK cells as described above (Fig. S3). The I_{K1} formulations used were as follows:

Control

$$I_{K1} = \frac{0.059764(V - E_K + 0.582854)}{0.754829 + e^{0.0767156(V - E_K + 0.582854)}} - 0.0114237$$

WT/E299V

$$I_{K1} = \frac{0.0301295(V - E_K - 0.532092)}{0.090999 + e^{0.0188999(V - E_K - 0.532092)}} + 0.008248$$

E299V

$$I_{K1} = 0.0166814(V - E_K + 0.0118494) - 6.6243 \times 10^{-5}(V - E_K + 0.0118494)^2 + 0.034651.$$

The APD restitution of the modified model was matched to the original published model (6).

Computer Simulations. The steady-state cardiac action potentials in all cases were obtained by pacing the ionic models for 50 s at 1 Hz. The human VM model was used to study the propagation of the cardiac impulse in a cable-like rectangular lattice of area 2 × 0.03 cm, with a resolution of 100 μm and no-flux boundary conditions at the edges. The strand was divided into two cell types, namely, endocardial (1 × 0.03 cm) and epicardial (1 × 0.03 cm), connected to each other to introduce electrical heterogeneity. The strand was paced from the endocardial end at 2 Hz for 10 s and pseudo-ECGs were calculated (12) for all mutations (ORd-control, ORd-WT/E299V, ORd-E299V, ORd-WT/D172N, and ORd-D172N). The propensity to reentry in the presence of these mutations was studied in human VM as well as atria models by artificially initiating a spiral wave (S1–S2 cross-field protocol) in a 2D sheet of tissue (6 × 6 cm). Vulnerability grids were constructed based on outcome for a range of S1–S2 intervals.

Three-Dimensional Anatomical Computer Modeling. We further investigated the possible mechanisms of arrhythmia initiation and maintenance in the presence of E299V mutation using a 3D anatomical model of rabbit ventricles. The model consisted of 547,680 myocardial nodes (862,515 nodes including bath and blood cavities), with an average internodal spacing of 250 μm, which was sufficient for convergence of propagation (13). A branching His-Purkinje system (PS) was implemented, as described elsewhere (14), with endpoints inserted into the myocardium up to one-third of the wall thickness. Sodium conductance, tissue conductivities, gap junction resistances, and Purkinje-myocardium junction resistances were adjusted to correctly reproduce normal ventricular activation patterns recorded during sinus rhythm (15). Cardiac electrical activity was described by the bidomain representation of cardiac tissue, which accounts for both intra- and extracellular potential fields (ϕ_i and ϕ_e, respectively), linked by the transmembrane current density (I_m) (16). Ion dynamics for the myocardium were described by the rabbit VM action potential model developed by Mahajan et al. (17), whereas the model of Aslanidi et al. (18) was used to represent Purkinje cells. I_{K1} E299V mutations were implemented in both ventricular and Purkinje models as follows:

$$I_{K1} = 0.06634(V - E_K + 6.5) - 2.44009 \times 10^{-4}(V - E_K)^2 + 0.51383.$$

Simulations were performed to reproduce the ECGs during normal sinus rhythm in control and E299V. The consequences of

this mutation were also studied in simulations in which the peak sodium current was reduced by 20% to address the possibility that slight changes in cardiac excitability, for example as a result of mild hyperkalemia as might occur during exercise, could result in ventricular arrhythmias in this patient. All simulations were performed in a parallel Linux cluster environment provided by Teragrid computing facilities and the Ohio Supercomputer Center facilities.

1. Ishihara K, Ehara T (2004) Two modes of polyamine block regulating the cardiac inward rectifier K+ current IK1 as revealed by a study of the Kir2.1 channel expressed in a human cell line. *J Physiol* 556(Pt 1):61–78.
2. Panama BK, McLerie M, Lopatin AN (2007) Heterogeneity of IK1 in the mouse heart. *Am J Physiol Heart Circ Physiol* 293(6):H3558–H3567.
3. Pegan S, et al. (2005) Cytoplasmic domain structures of Kir2.1 and Kir3.1 show sites for modulating gating and rectification. *Nat Neurosci* 8(3):279–287.
4. Wilson IA, et al. (1984) The structure of an antigenic determinant in a protein. *Cell* 37(3):767–778.
5. Evan GI, Lewis GK, Ramsay G, Bishop JM (1985) Isolation of monoclonal antibodies specific for human c-myc proto-oncogene product. *Mol Cell Biol* 5(12):3610–3616.
6. O'Hara T, Virág L, Varró A, Rudy Y (2011) Simulation of the undiseased human cardiac ventricular action potential: model formulation and experimental validation. *PLOS Comput Biol* 7(5):e1002061.
7. Viswanathan PC, Shaw RM, Rudy Y (1999) Effects of IKr and IKs heterogeneity on action potential duration and its rate dependence: A simulation study. *Circulation* 99(18):2466–2474.
8. Priori SG, et al. (2005) A novel form of short QT syndrome (SQT3) is caused by a mutation in the KCNJ2 gene. *Circ Res* 96(7):800–807.
9. Grandi E, et al. (2011) Human atrial action potential and Ca2+ model: Sinus rhythm and chronic atrial fibrillation. *Circ Res* 109(9):1055–1066.
10. Gelband H, Bush HL, Rosen MR, Myerburg RJ, Hoffman BF (1972) Electrophysiologic properties of isolated preparations of human atrial myocardium. *Circ Res* 30(3): 293–300.
11. Workman AJ, Kane KA, Rankin AC (2001) The contribution of ionic currents to changes in refractoriness of human atrial myocytes associated with chronic atrial fibrillation. *Cardiovasc Res* 52(2):226–235.
12. Cerrone M, et al. (2007) Arrhythmogenic mechanisms in a mouse model of catecholaminergic polymorphic ventricular tachycardia. *Circ Res* 101(10):1039–1048.
13. Deo M, Boyle PM, Kim AM, Vigmond EJ (2010) Arrhythmogenesis by single ectopic beats originating in the Purkinje system. *Am J Physiol Heart Circ Physiol* 299(4): H1002–H1011.
14. Vigmond EJ, Clements C (2007) Construction of a computer model to investigate sawtooth effects in the Purkinje system. *IEEE Trans Biomed Eng* 54(3):389–399.
15. Boyle PM, Deo M, Plank G, Vigmond EJ (2010) Purkinje-mediated effects in the response of quiescent ventricles to defibrillation shocks. *Ann Biomed Eng* 38(2): 456–468.
16. Vigmond EJ, Weber dos Santos R, Prassl AJ, Deo M, Plank G (2008) Solvers for the cardiac bidomain equations. *Prog Biophys Mol Biol* 96(1-3):3–18.
17. Mahajan A, et al. (2008) A rabbit ventricular action potential model replicating cardiac dynamics at rapid heart rates. *Biophys J* 94(2):392–410.
18. Aslanidi OV, Sleiman RN, Boyett MR, Hancox JC, Zhang H (2010) Ionic mechanisms for electrical heterogeneity between rabbit Purkinje fiber and ventricular cells. *Biophys J* 98(11):2420–2431.

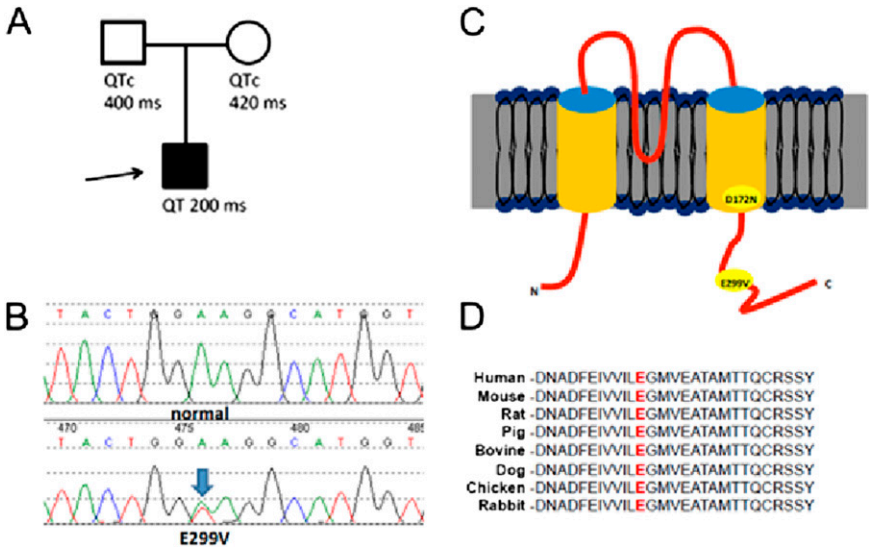

Fig. S1. (*A*) Family pedigree. The arrow indicates the clinically and genetically affected proband (black symbol); empty symbols indicate the clinically and genetically unaffected parents. (*B*) DNA sequence for a normal control and for the index patient. The arrow indicates the affected codon. (*C*) Cartoon of the predicted transmembrane topology of the Kir2.1 channel showing the location of E299V and D172N. (*D*) Amino acid sequence alignment of Kir2.1 channels from various species in the region surrounding codon 299 (highlighted). A remarkable level of conservation is evident, suggesting the functional relevance of this region.

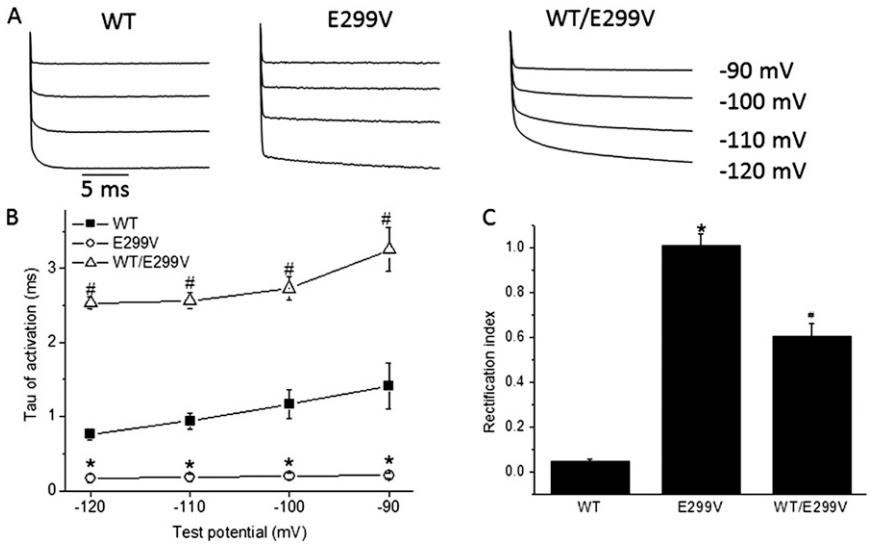

Fig. S2. Activation kinetics and rectification index. (*A* and *B*) The activation phases were fitted with single exponential functions and the time constants (taus) of the fittings are plotted (n = 7–10 cells for each group), $^{*}P < 0.05$, vs. WT and WT/E299V; $^{\#}P < 0.05$ vs. WT. (*C*) Rectification index for WT, E299V, and WT/E299V. The rectification index was calculated by dividing the value of the outward currents measured at 0 mV by the absolute value of the inward currents measured at −100 mV (n = 7–9 cells for each group), $^{*}P < 0.05$, vs. WT and WT/E299V; $^{\#}P < 0.05$ vs. WT.

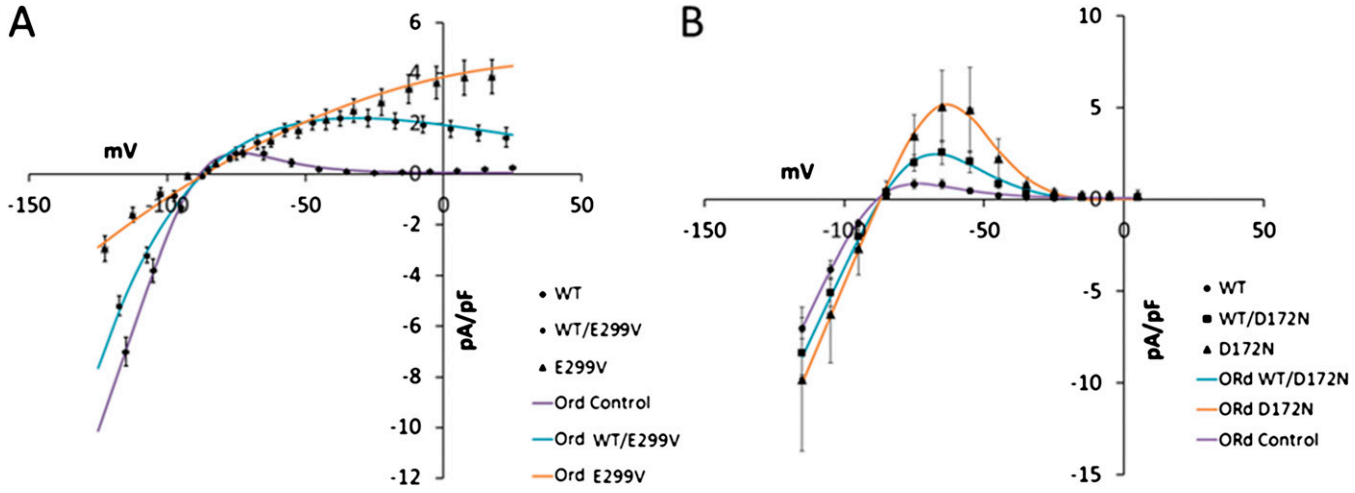

Fig. S3. I_{K1} formulations in the human ventricular cell model (ORd) were fitted to match the experimental current–voltage relationships in (*A*) WT, WT/E299V, and E299V, and (*B*) WT, WT/D172N, and D172N.

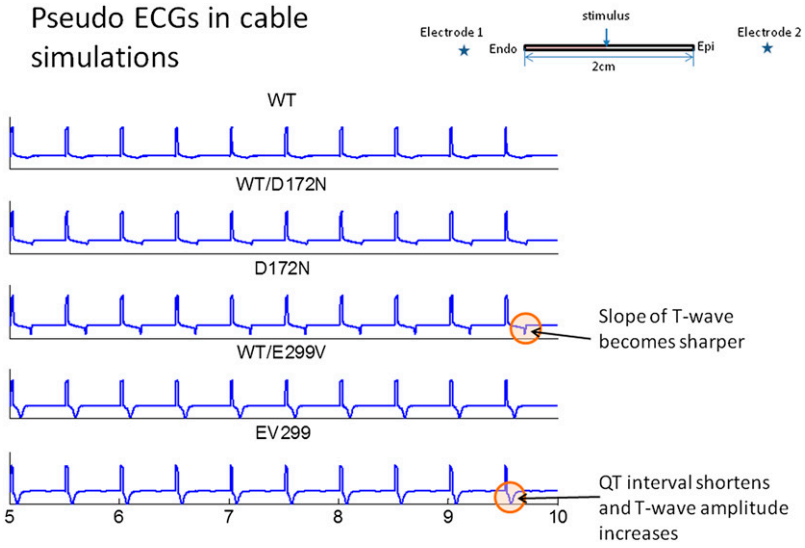

Fig. S4. Simulated lead-II ECGs during propagation of excitation in a cable for control (WT) and SQT3 mutations under consideration. The simulation protocol is shown at the top.

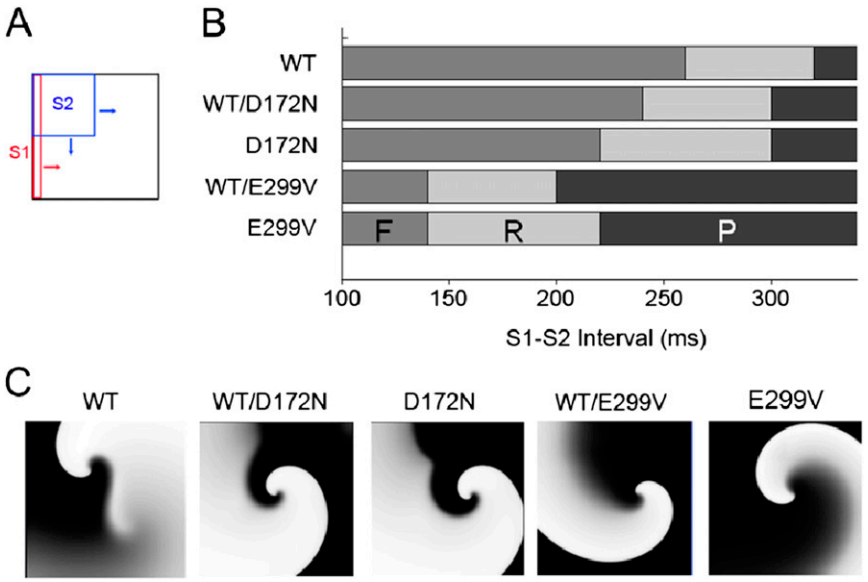

Fig. S5. (*A*) Cross-field S1–S2 stimulation protocol used to investigate vulnerability to reentry. (*B*) Vulnerability to reentry grid constructed by summarizing the outcome at varying S1–S2 intervals. F, failure to conduct S2 stimulus; P, normal propagation of S2 beat; R, reentry. (*C*) Snapshots of spiral wave reentry obtained in control (WT) and all SQT3 mutations.

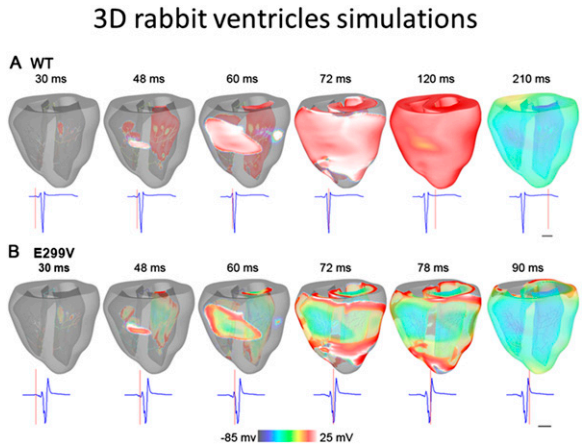

Fig. S6. Three-dimensional simulations using rabbit ventricular geometry. A typical excitation sequence during sinus rhythm is shown for (*A*) control and (*B*) E299V along with the corresponding simulated ECGs. Colors represent transmembrane voltages. (Horizontal scale bar, 50 ms.)

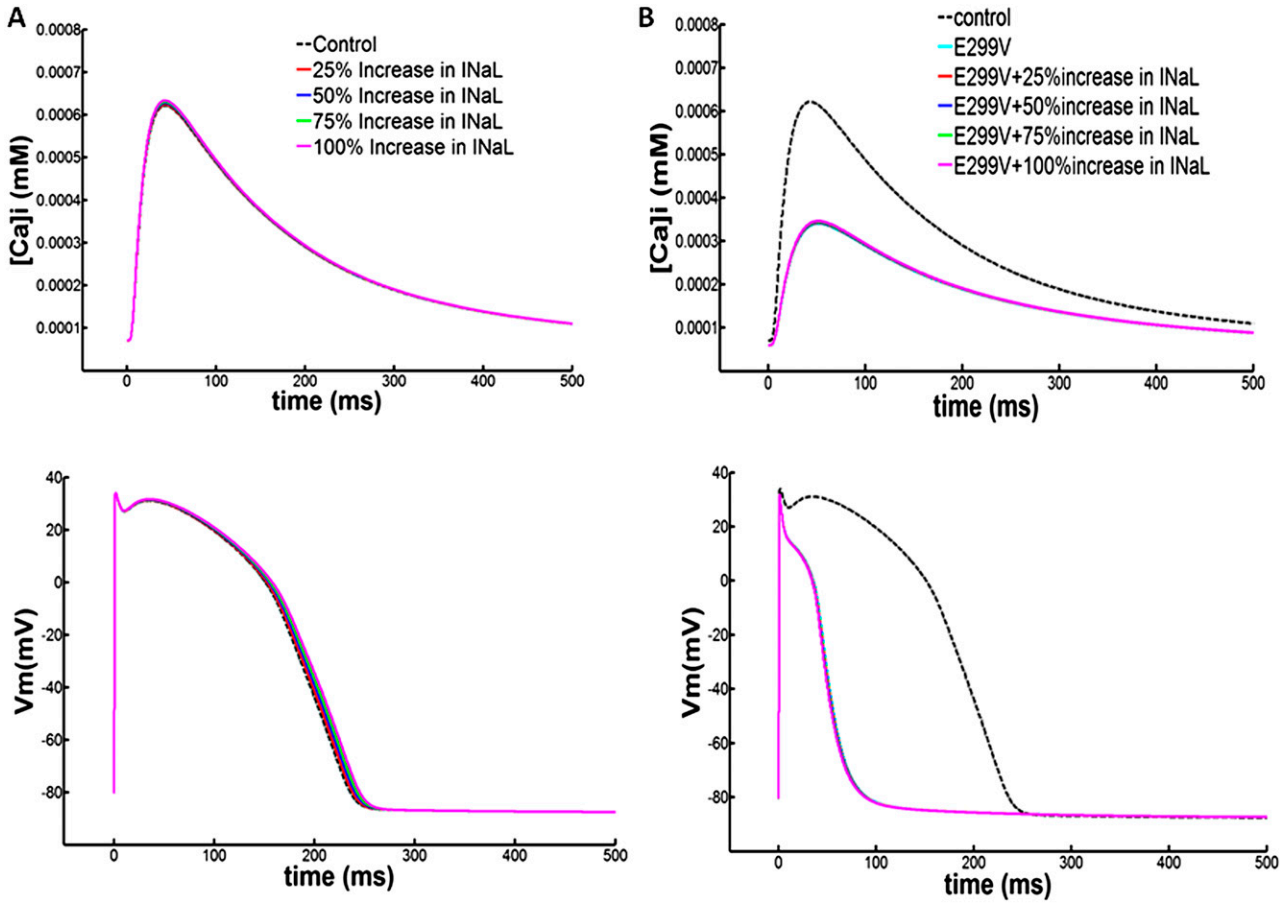

Fig. S7. Simulation results showing the effects of I_{NaL} increase on the intracellular calcium transient (*Upper*) and the action potential duration measured at 80% repolarization (APD_{80}). (*A*) Control. Increasing I_{NaL} up to 100% produces negligible changes in the intracellular calcium transient and APD_{80}. (*B*) E299V. Increasing I_{NaL} up to 100% produces no change in the voltage-dependent intracellular calcium transient or APD_{80} as a result of the exceedingly large outward I_{K1}, which overpowers any amount of inward depolarizing current coming through the I_{Na} channel during the plateau.

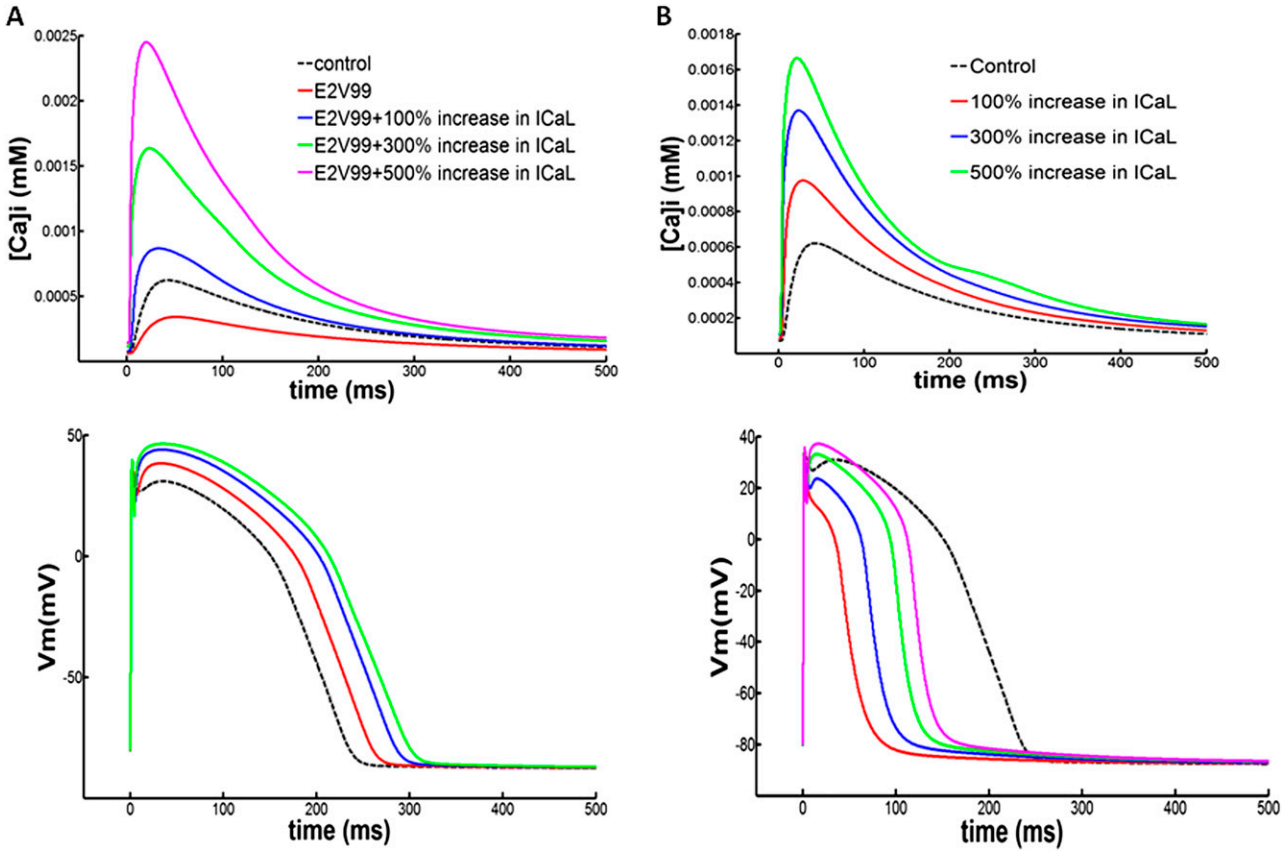

Fig. S8. Simulation results showing the effects of I_{CaL} increase on the intracellular calcium transient (*Upper*) and the action potential duration measured at 80% repolarization (APD_{80}). (*A*) Control. Increasing I_{CaL} up to 500% led to progressive increases in the intracellular calcium transient and APD_{80}. (*B*) E299V. Increasing I_{CaL} 100% restored the originally reduced calcium transient above control levels, increased the action potential plateau, and slightly restored the APD toward control. Increasing I_{CaL} by 300 and 500% further prolonged the APD to some extent but produced large increases in the intracellular calcium transient.

Table S1. Effects of increasing I_{NaL} in the control on APD_{90} and Intracellular Ca^{2+}

I_{NaL}, %	APD_{90} prolongation, %	Ca transient amplitude increase, %
125	1	0.47
150	2.04	0.90
175	3.09	1.45
200	4.10	1.07

Table S2. Effects of increasing I_{NaL}in the E299V on APD_{90} and Intracellular Ca^{2+}

I_{NaL}, %	APD_{90} prolongation, %	Ca transient amplitude increase, %
125	0.50	0.45
150	1.17	0.88
175	1.80	1.32
200	2.40	1.77

Table S3. Effects of increasing I_{CaL} in the control on APD_{90} and Intracellular Ca^{2+}

I_{CaL}, %	APD_{90} prolongation, %	Ca transient amplitude increase, %
200	10.496	56.94
400	21.298	120.487
600	27.439	168.096

Table S4. Effects of increasing I_{CaL} in the E299V on APD_{90} and Intracellular Ca^{2+}

I_{CaL}, %	APD_{90} prolongation, %	Ca transient amplitude increase, %
200	35.12	154.54
400	70.89	427.412
600	94.91	733.88